Enhancing high-temperature strength of (B$_4$C+Al$_2$O$_3$)/Al designed for neutron absorbing materials by constructing lamellar structure

Y.N. Zan [a,c,1], Y.T. Zhou [a,1], H. Zhao [a], Z.Y. Liu [a], Q.Z. Wang [b,**], D. Wang [a], W.G. Wang [a], B. L. Xiao [a], Z.Y. Ma [a,*]

[a] *Shenyang National Laboratory for Materials Science, Institute of Metal Research, Chinese Academy of Sciences, 72 Wenhua Road, Shenyang, 110016, China*
[b] *Key Laboratory of Nuclear Materials and Safety Assessment, Institute of Metal Research, Chinese Academy of Sciences, 72 Wenhua Road, Shenyang, 110016, China*
[c] *School of Materials Science and Engineering, University of Science and Technology of China, 72 Wenhua Road, Shenyang, 110016, China*

ARTICLE INFO

ABSTRACT

Aiming at developing new generation of high-temperature neutron absorbing materials for both structural and functional usages, (B$_4$C + Al$_2$O$_3$)/Al composites were fabricated. Hot forging and extruding were carried out to adjust the microstructures of the composites. The forged samples exhibited a lamellar structure with Al$_2$O$_3$ staying at the grain boundaries. In the extruded sample, most Al$_2$O$_3$ entered into the interior of ultrafine-grains. Different strengthening effects of intergranular and intragranular Al$_2$O$_3$ at room and high temperatures were studied. It was verified that Al$_2$O$_3$ distributed at the grain boundaries was more beneficial to enhance the high-temperature strength by strengthening the grain boundaries and preventing dislocations from annihilating, therefore the forged samples were much stronger than the extruded sample at 375 °C. The sample forged with a height reduction ratio of 8:1 showed an ultimate strength of 342 MPa at room temperature and an ultimate strength of 96 MPa at 375 °C.

1. Introduction

B$_4$C is widely used in aluminium matrix composites (AMCs) for its low density (2.51 g/cm^3), high modulus (445 GPa) and other excellent properties [1–4]. Moreover, since ^{10}B isotope has a high thermal neutron absorption cross-section (3837 b), B$_4$C/Al composites become a kind of appealing neutron absorbing materials in nuclear industries [1,5,6].

The dry storage is an important storage mode for the spent nuclear fuel. For practical application, the service condition can be up to 350 °C for a long time [7]. Thus, one crucial requirement is the stable high-temperature strength during the long-term service. However, the conventional B$_4$C/6xxx and B$_4$C/1xxx composites are not strong enough for serving at such high temperatures [8,9] and extra supporting steel structures are usually required, which are detrimental to heat dissipation and weight reduction. So developing B$_4$C/Al composites with enough high-temperature strength is of great significance for safety and economy.

Al–Si–Cu or Al–Si–Mg series heat-resistant alloys [10–12] are widely used in the automotive field. Their high-temperature strength relies mainly on heat treatment and consequent precipitated phases, which would coarsen or dissolve at high temperature over 250 °C [13–16]. Therefore, these alloys are incompetent for high-temperature service conditions like spent fuel dry storage. By adding Sc and Zr into the B$_4$C/Al composites, the strength of the composites at 350 °C was increased to about 40 MPa [7]. It was still far below the engineering requirement (about 90 MPa at 350 °C according to Ref. [17]).

Compared to the strengthening precipitates in Al alloys, most ceramic reinforcements are extremely stable at high temperature. It has been reported that the nano-scale ceramic particles exhibited excellent strengthening effect on the high-temperature strength [8,12]. A kind of high-temperature Al material known as sintered aluminium powder (SAP) was developed in the 1950s [18]. The strength of SAPs at high temperatures is improved by the nanoscale Al$_2$O$_3$ introduced from flaky Al powder surfaces. Therefore, it is a promising route to fabricate the B$_4$C/Al composites for high-temperature structural applications by introducing this method.

For SAPs, in order to obtain the demanded high-temperature strength, the Al_2O_3 content as high as 10 wt% was required [18,19]. In this case, considering the Al_2O_3 thickness as 10 nm [20], the flaky Al powders as thin as 200 nm must be used. Such thin Al flakes would increase the inflammability and decrease the loose density, which inhibits the practical application significantly. In order to reduce the negative effect of excessive Al_2O_3 addition on the composite fabrication, it is necessary to increase the strengthening efficiency of Al_2O_3 in SAPs. However, because of the lack of sophisticated characterization methods at that time, the morphology and distribution of Al_2O_3 were unknown. As a result, the strengthening mechanisms in SAPs were unclear and strengthening efficiency of Al_2O_3 was hard to increase further.

The strengthening effects of the reinforcements in metal matrix composites can be divided into two categories, i.e. direct strengthening by load transfer and indirect strengthening by dislocation accumulation [21]. Furthermore, since the stability of grain boundaries is more important under high temperatures [22], strengthening the grain boundaries may be of great importance. All these strengthening mechanisms are closely related to the reinforcement morphology and distribution, in especial, for flaky reinforcements [23,24]. So adjusting the morphology and distribution of Al_2O_3 may be helpful to clarify the key factors influencing the strengthening efficiency in SAPs.

In this study, SAP method was applied to fabricate $(B_4C + Al_2O_3)/Al$ composites with a relatively low Al_2O_3 content. Hot forging and extruding were carried out to adjust the morphology and distribution of Al_2O_3. The aim of this study is (a) to develop new neutron absorbing materials with excellent high-temperature strength for dry storage of the spent nuclear fuel and (b) to identify factors responsible for the mechanical properties at both room temperature (RT) and high temperature. By means of sophisticated structural characterization and strengthening mechanism analysis, it was confirmed that the lamellar structure in which Al_2O_3 was located at the Al grain boundaries exhibited the best strengthening effect at high temperatures.

2. Experimental procedure

2.1. Preparation of composites

The $(B_4C + Al_2O_3)/Al$ composites were fabricated using commercial sphere-shaped pure aluminium powders (99.5% purity) and granular-shaped B_4C particles (96.5% purity) as raw materials. The mean sizes of original aluminium powders and B_4C particles were 5 μm and 6.5 μm, respectively.

Al powders were ball milled in argon atmosphere using an attritor with a ball-to-powder ratio (BPR) of 15:1 at 300 rpm for 3 h to obtain the flaky powders, after which passivation was carried out to introduce Al_2O_3 film. Then ball-milled Al powders were mechanically mixed with 10 wt% B_4C particles in a bi-axis rotary mixer for 8 h at a rotational rate of 50 rpm and a BPR of 1:1.

The as-mixed powders were cold compacted under a pressure of 70 MPa and then hot pressed into billets with a height of 80 mm and a diameter of 65 mm, under a pressure of 50 MPa in a vacuum chamber of 10^{-2} Pa at 630 °C for 2 h. Then different hot working processes were carried out at 450 °C, including forging with a height reduction ratio of 4:1 (sample F4), 8:1 (sample F8), 16:1 (sample F16), and extruding with an extrusion ratio of 16:1 (sample E16).

2.2. Characterization

Flaky Al powders were characterized using Micromeritics ASAP2010 M in liquid nitrogen to determine the specific surface area according to Brunauer-Emmett-Teller (BET) analyses and the oxygen content of powders was measured using LECO TCH600 to calculate Al_2O_3 mass fraction.

The microstructure of the composites was observed using optical microscopy (OM, Zeiss Axiovert 200MAT), field emission scanning electron microscopy (FESEM, Leo Supra 55) and transmission electron microscopy (TEM, FEI Tecnai F30). Specimens for OM observation were ground with 3000 grit abrasive paper and then mechanically polished using diamond paste. After polish, the specimens were further ion etched using Leica RES101 to remove impurities. Specimens for TEM were prepared by metallographic grinding and dimpling, followed by ion-milling using a Gatan PIPS (Model 695). The forged samples were observed perpendicular to the forging direction while the extruded sample was observed along the extrusion direction.

2.3. Mechanical property test

Tensile specimens with a gauge length of 5 mm, a width of 1.7 mm and a thickness of 1.2 mm were machined from the composites. For the forged composites, the tensile specimens were cut from the forged disks with the axis parallel to the radial direction of the disks. For the extruded composite, the tensile specimens were cut parallel to the extrusion direction. Tensile testing was carried out at a strain rate of 1×10^{-3} s^{-1} at both RT and 375 °C using an Instron 5582 tester after being annealed at 450 °C for 4 h and then cooled inside the furnace. To observe the microstructure of specimens after tensile testing, larger tensile specimens with a gauge length of 10 mm, a width of 3 mm and a thickness of 2.5 mm were tested, and the fractured specimens were immediately quenched after testing at 375 °C. Then specimen was sampled near the cracked point for TEM observation.

2.4. Statistical analysis

For density measurement of each sample, 3 specimens were used and repeated experiments were carried out for 3 times for each specimen. Average lamellae thickness/grain size of the composites was obtained by counting over 120 grains for each composite. Average length of Al_2O_3 was obtained by counting the length of over 50 Al_2O_3 for each sample. For tensile testing, at least 5 tensile specimens were tested for each composite.

3. Results

3.1. Characterization of the flaky Al powders

The SEM image of the mixture of flaky powders and B_4C particles is shown in Fig. 1. Al powders exhibited a flaky morphology with irregular and rolled-up edges, while the B_4C particles exhibited a granular morphology with straight edges. The characterization results of the flaky Al powders are listed in Table 1. The thickness was calculated according to the BET using the relation $Thickness_{BET} = 2/(BET * \rho_{Al\ flake})$, where BET is the specific surface area of the flaky Al powders (2.12 m^{2}g^{-1}) and $\rho_{Al\ flake}$ is the density of the flaky powder.

Taking the thickness of Al_2O_3 film as 10 nm (according to Ref. 19 and the present study shown in Fig. 4), $\rho_{Al\ flake}$ can be expressed as $\rho_{Al} *$ $(1–20/Thickness_{BET}) + \rho_{Al_2O_3} * 20/Thickness_{BET}$, where ρ_{Al} (2.7 g/cm^3) and
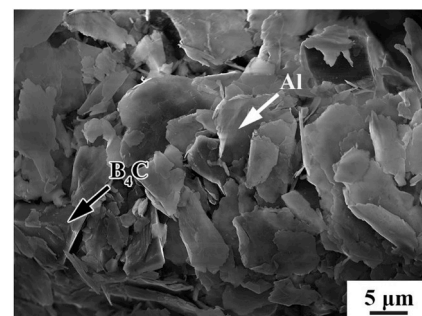

Fig. 1. SEM image of the mixture of Al powders and B_4C particles.

Table 1
Characteristics of the ball-milled Al powders.

BET ($m^2 g^{-1}$)	Thickness$_{BET}$ (nm)	Al_2O_3 (vol%)	O (wt.%)	Al_2O_3 (wt.%)
2.12	347	5.8	3.0	6.3

$\rho_{Al_2O_3}$ (2.9 g/cm^3) are the density of Al and amorphous Al_2O_3 [25]. So the volume fraction of Al_2O_3 was calculated to be 5.8 vol%. The oxygen content of the flaky powders was measured as 3.0 wt% on LECO TCH600, so the corresponding Al_2O_3 content was 6.3 wt%. The volume fraction corresponding to 6.3 wt% can be calculated as $(6.3/2.9)/(6.3/2.9 + 93.7/2.7) = 5.9$ vol%, which was in accord with the volume fraction calculated by BET analyses.

3.2. Density of the composites

Density values of the composites are given in Table 2. Because the amount of γ-Al_2O_3 transformed from amorphous Al_2O_3 was unknown, the theoretical density of these composites cannot be determined. However, it can be seen that the density of the composites was improved by increasing the deformation amount. Forging at a reduction ratio of 4:1 is an ordinary deformation process and could obtain completely densified samples for other composites [26]. However, it was proven to be insufficient for the present (B_4C + Al_2O_3)/Al composites and the density of sample F4 (2.664 g/cm^3) was about 1.2% lower than that of sample E16 (2.697 g/cm^3). This was because Al_2O_3 films located at the flaky powder surfaces made the sintering and bonding more difficult [27]. Only by high-ratio deformation could Al_2O_3 be disrupted, after which the Al matrix inside the powders could contact and bond mutually.

3.3. Microstructure

Under the dark filed of the OM observation, the edges of the particles can be exhibited clearly, making them distinct from the micro-cavities. As shown in Fig. 2, micro-cavities in sample F4 (Fig. 2a) located possibly at the flake/flake boundaries could be seen, which agreed with the density measuring results. The cavities resulted from poor sinterability of the flaky powders due to surface oxide layer [27]. The cavity ratios were reduced in samples F16 and E16 due to larger deformation ratio, as shown by Fig. 2b and c.

According to the TEM observations, some main differences in various composites are listed in Table 3. Fig. 3 shows the TEM images of the forged samples. The grains exhibited the lamellar shape in these forged samples. The interlamellar spacing decreased with increasing the forging ratio from 4:1 to 16:1, and the average thicknesses of the lamellar grains of samples F4, F8 and F16 were estimated to be about 326 nm, 201 nm and 86 nm, respectively (Fig. 3a–c). The STEM image of sample F4 is shown in Fig. 3d and the EDS mapping (the insets of Fig. 3d) revealed that the light lines in the STEM images were corresponding to Al_2O_3 layers on the surfaces of the flaky powders.

Fig. 4 shows Al_2O_3 in the forged samples. It could be seen that Al_2O_3 films were mainly distributed at the grain boundaries and constituted the lamellar structure with the Al grains. According to Balog et al. [28, 29], the lamellar morphology was corresponding to the characteristic of amorphous Al_2O_3 (am-Al_2O_3). The average length of am-Al_2O_3 was found to slightly decrease with increasing the forging ratio, which was 373 nm in sample F4 (Figs. 4a) and 307 nm in sample F16 (Fig. 4b). The high resolution TEM (HRTEM) image in Fig. 4c confirmed the amorphous nature of the Al_2O_3 layer. The lamellar amorphous Al_2O_3 had a thickness of about 10 nm.

Besides lamellar am-Al_2O_3, some Al_2O_3 with granular morphology were also found (Fig. 4d). The corresponding selected-area electron diffraction (SAED) pattern is given in Fig. 4d as well. The diffraction pattern could be indexed by the [110] zone-axis of an fcc lattice with a lattice parameter a = 7.93 nm. This suggests that the aluminium oxide particle was γ-Al_2O_3 (space group $Fd\bar{3}m$). The weak spot l = 2n in the [110] SAED partern confirmed the d glide in (100) plane. The γ-Al_2O_3 particles exhibited the same morphology and size as it was found in other investigations [28,29].

γ-Al_2O_3 was verified to transform from am-Al_2O_3 during the high-temperature sintering process [28]. During this process, the thickness of am-Al_2O_3 can reach a certain value by diffusion, then transition will happen because the higher bulk Gibbs free energy of am-Al_2O_3 compared to that of γ-Al_2O_3 can be compensated by the lower sum of surface and interfacial energies [30]. It should be noted that only a small amount of Al_2O_3 was transformed into γ-Al_2O_3 and most of the Al_2O_3 remained the amorphous type in the present study.

TEM image shows a well-bonded interface between B_4C and Al and moderate interfacial reaction (Fig. 5a). The higher-magnification TEM image and the corresponding SAED pattern confirmed that the reaction product was Al_3BC (Fig. 5b), which resulted from the reaction between B_4C and Al, and was also found in the B_4C/6061Al composites [31].

Fig. 6a shows the TEM image of sample E16. An ultrafine-grained structure was developed after the extrusion process, which made it distinctly different from that of the forged samples. The average grain size of sample E16 was 223 nm. From the TEM and STEM images of sample E16 shown in Fig. 6b and c, it can be seen that after extrusion, Al_2O_3 flakes were distributed randomly and most of them entered into the Al grains. The average length of Al_2O_3 in the extruded sample was 96 nm, which was much shorter than that in the forged samples.

The microstructural differences in the forged and extruded samples are attributed to different deforming modes. The relatively simpler deforming mode in the forging process could only make Al_2O_3 extend with the Al powders perpendicular to the forging direction. Al grain boundaries could not pass Al_2O_3 by grain growth, so Al_2O_3 stayed at the boundaries even after 16:1 forging, as shown in Fig. 4a and b. In the extrusion process, much more complicated material flow caused drastic torsion and tearing of the Al powders, resulting in that Al_2O_3 was divorced from the grain boundaries and entered into the Al grains, as shown in Fig. 6a–c.

TEM observations showed that the interface bonding and reaction at the B_4C/Al interface in the extruded sample were similar to that in the forged samples, and γ-Al_2O_3 was also found in sample E16 (not shown).

In the forging process, dislocation activities were involved and the grain boundaries were formed parallel to the forging direction (Fig. 7a).
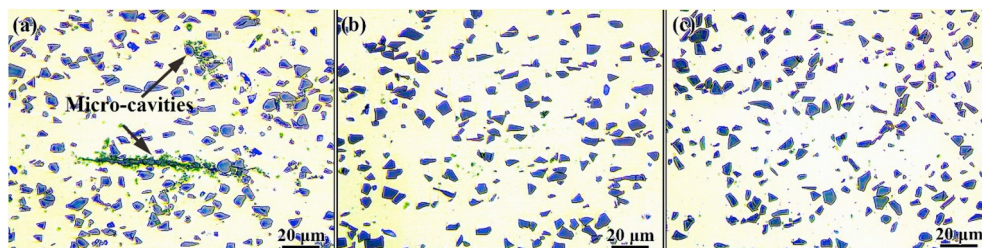

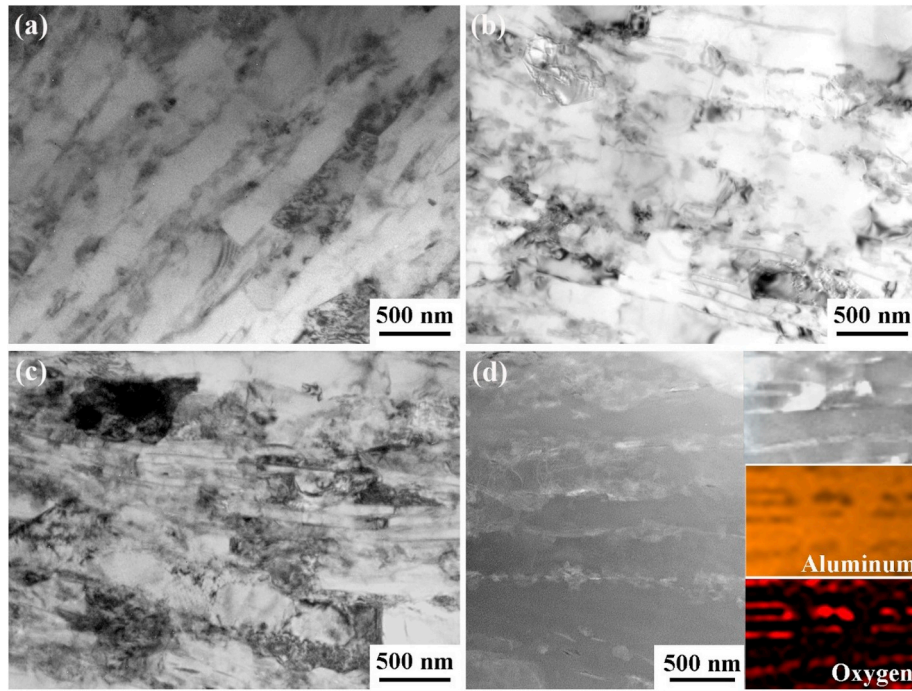**Fig. 2.** OM images of samples (a) F4, (b) F16 and (c) E16.

Fig. 3. TEM images showing lamellar structure of samples (a) F4, (b) F8, (c) F16 and (d) STEM image of sample F4.
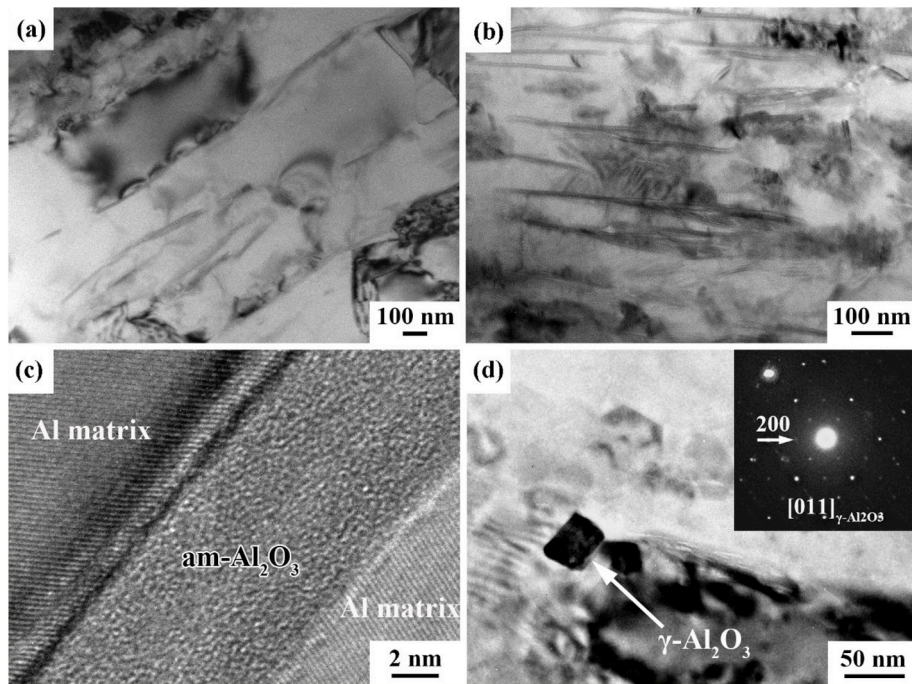

Fig. 4. TEM images showing lamellar Al_2O_3 in (a) sample F4 and (b) sample F16; (c) magnified view of amorphous Al_2O_3 and (d) γ-Al_2O_3 particle with inset SAED pattern in both samples.

Table 2
Density of (B_4C + Al_2O_3)/Al composites.

Sample	F4	F8	F16	E16
Density (g/cm3)	2.664 ± 0.005	2.678 ± 0.002	2.683 ± 0.002	2.697 ± 0.001

Table 3
Grain and Al_2O_3 characteristics of (B_4C + Al_2O_3)/Al composites.

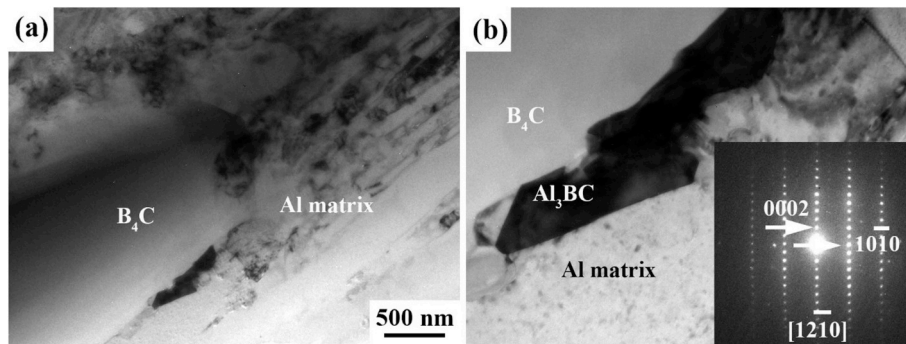| Sample	Lamellae thickness/grain size (nm)	Al_2O_3 length (nm)
F4	326 ± 147	373 ± 160
F8	201 ± 86	314 ± 143
F16	86 ± 33	307 ± 139
E16	223 ± 71	96 ± 34

Fig. 5. TEM images showing (a) B_4C in sample F16 and (b) Al_3BC formed at B_4C/Al interface and the corresponding SAED pattern (inset).
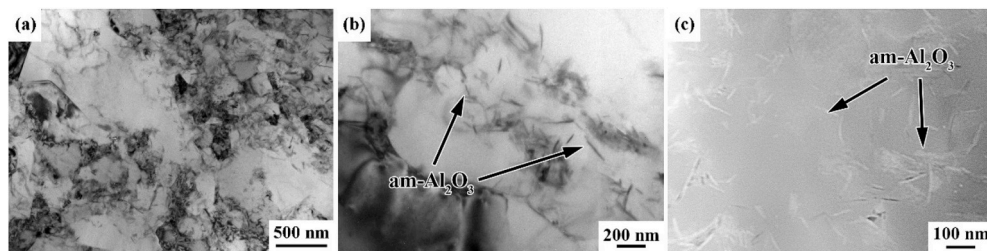

Fig. 6. (a) TEM image showing ultrafine-grained structure, (b) TEM and (c) STEM images showing intragranular distribution of Al_2O_3 in sample E16.

In TEM images with high magnification, most dislocations were found to confine by the adjacent Al_2O_3 films and propagate along the lamellae (Fig. 7b). These dislocations finally piled-up in front of the grain boundaries. In a single Al layer, sub-grain boundaries were developed, shown as the dislocation array perpendicular to the lamella boundary (Fig. 7c).

In the case of the extruded sample, Fig. 8a and b shows the same view field in sample E16 using HAADF-STEM and bright-field TEM images, respectively. The image contrast of HAADF-STEM mode is determined by the chemical compositions of the imaged area and seldom influenced by lattice strains (e.g. dislocations). Combining the two imaging modes, it can be clearly seen that dislocations accumulated at the grain boundaries and tangled the intragranular Al_2O_3. This suggests that the dislocation activity in this sample was mainly impeded by the grain boundaries and Al_2O_3 flakes.

3.4. Mechanical properties

Fig. 9 shows the tensile stress–strain curves of the composites and the mechanical properties are listed in Table 4. At RT (Fig. 9a), for the forged samples, the strength increased with increasing the forging ratio. Sample F4 showed a relatively low strength and ductility because of the low relative density. Further increase in the deformation ratio resulted in denser composites, and therefore sample F8 exhibited simultaneous improvement in strength and ductility compared to sample F4. When the

forging ratio increased to 16:1, sample F16 was further strengthened, but with lower ductility, attributable to poor strain hardening capability of the finer grains [32]. As for the extruded sample, the strength of sample E16 was close to that of sample F8. In general, the strength of annealed B_4C/Al composites using 1xxx or 6xxx alloys as the matrices is lower than 150 MPa [7,8,33], which confirmed the significant strengthening effect of Al_2O_3

At 375 °C (Fig. 9b), all the samples exhibited significant strength decline. However, the present $(B_4C + Al_2O_3)/Al$ composites had higher strength compared to previous B_4C/Al composites with the yield strength lower than 40 MPa [7,9].

From Fig. 9b, it can be seen that the high-temperature strength of the composites closely depended on the microstructure. For the forged samples with the lamellar structure, sample F8 showed the highest tensile strength of 96 MPa while the strength of more uniform-structured extruded sample E16 was only 58 MPa. This indicates that the lamellar structure was more efficient to maintain the strength at this temperature.

3.5. Fractographs

As shown in Fig. 10, sample F8 exhibited mainly brittle fracture at RT, consistent with low ductility of the composite. The lamellar structure could be observed in Fig. 10a. Under a higher magnification as shown in Fig. 10b, cleavage-like facets were revealed, which might be
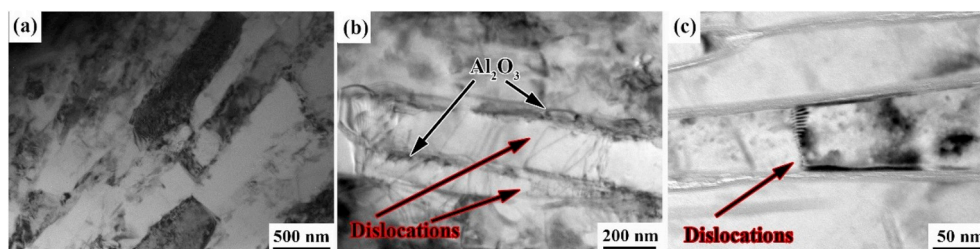

Fig. 7. TEM images showing (a) grain boundaries formed parallel to forging direction, (b) dislocations propagating along the lamellae, and (c) sub-grain boundaries developed by dislocation array perpendicular to the lamella boundary in sample F16.
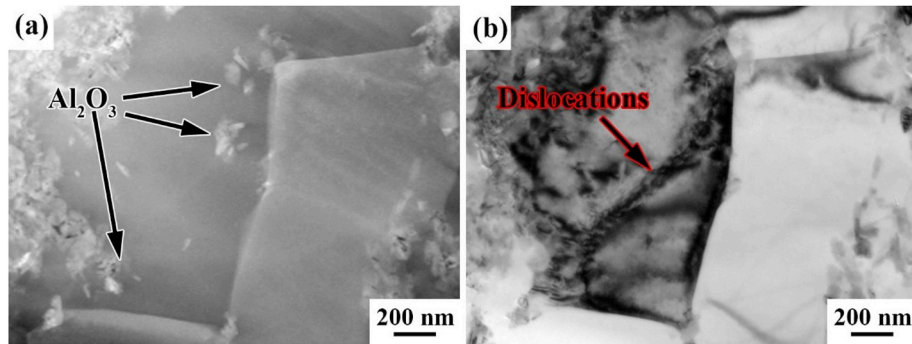
Fig. 8. (a) STEM and (b) TEM images showing Al_2O_3 and dislocation distribution in sample E16.
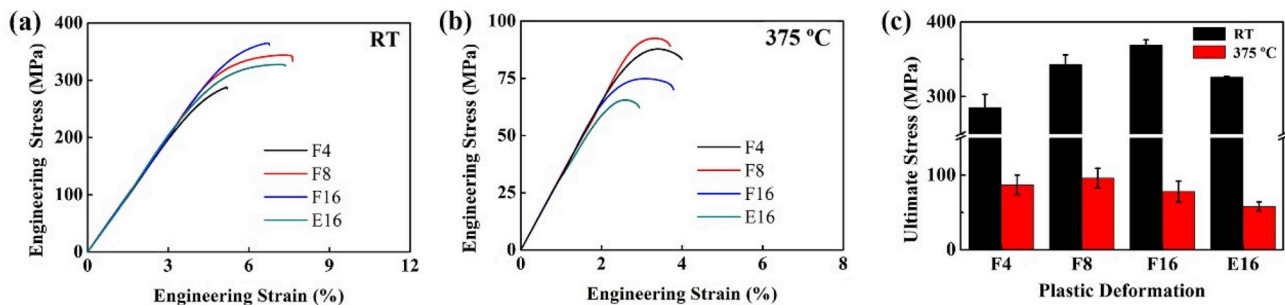

Fig. 9. Tensile stress-strain curves for various composites at (a) RT and (b) 375 °C and (c) ultimate strength values.

Table 4
Tensile properties of $(B_4C + Al_2O_3)/Al$ composites.

Sample	RT			375 °C		
	YS (MPa)	UTS (MPa)	El (%)	YS (MPa)	UTS (MPa)	El (%)
F4	258 ± 8	285 ± 6	1.0 ± 0.6	81 ± 10	87 ± 8	1.4 ± 0.5
F8	272 ± 6	342 ± 4	2.5 ± 0.3	95 ± 11	96 ± 4	0.9 ± 0.3
F16	331 ± 6	369 ± 3	1.4 ± 0.3	73 ± 7	78 ± 5	1.6 ± 0.4
E16	262 ± 2	326 ± 1	2.6 ± 0.2	57 ± 3	58 ± 3	1.0 ± 0.2

YS: Yield strength and UTS: Ultimate tensile strength.

the initiation points of fracture (black arrows). Al_2O_3 was observed to locate at the lamella boundaries in the forged samples (Fig. 10c). During tensile deformation at RT, stress concentration could form at the interfaces because of the huge difference in the deformation ability of Al and Al_2O_3. The irreconcilable deformation and stress concentration led to the exfoliation of Al_2O_3 and the initiation of fracture.

Fig. 11 shows the fracture surfaces of samples F8 and F16 at 375 °C.

Lamellar structure was also clearly observed. Compared to sample F8 (Fig. 11a), the lamellas in sample F16 (Fig. 11b) were shown to be thinner and more discontinuous. It is due to that severer forging deformation decreased the distance between Al_2O_3 along the forging direction and increased the distance perpendicular to the forging direction. This is proposed to be the reason why high-temperature strength of sample F8 was higher than that of sample F16.

Under a high magnification, Al_2O_3 could also be found (Fig. 11c), but it did not form a cleavage like the situation at RT (Fig. 10c). It is believed that at elevated temperatures, intergranular Al_2O_3 could pin the grain boundaries strongly so the grain boundaries could not glide easily during the tensile process, resulting in significantly increased strength. Al matrix was so soft at high temperature that the shear stress imposed on Al_2O_3 could not break Al_2O_3 or the interfaces. Thus, the fracture process could only initiate in the Al matrix. So the strengthening effect of intergranular Al_2O_3 could be effective until the final fracture.

The fracture surfaces for sample E16 are shown in Fig. 12. The fracture surface at RT exhibited a brittle manner and only small and shallow dimples were observed. No distinct lamellar fracture characteristic was detected (Fig. 12a), which was consistent with the TEM observations (Fig. 6). High-temperature fracture morphology of sample E16 is shown in Fig. 12b. The intergranular fracture mode dominated
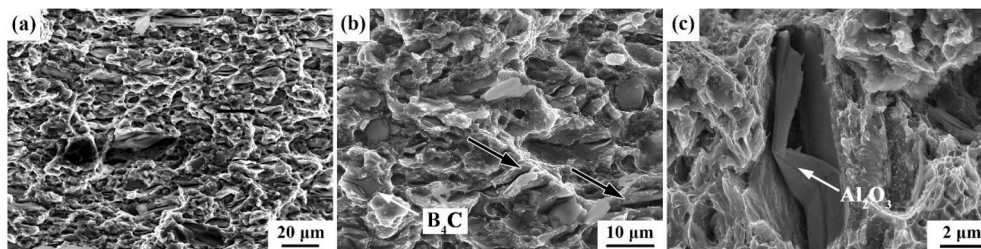

Fig. 10. SEM fractographs of sample F8 at RT showing (a) lamellar structure, (b) cleavage-like facets (black arrows) and (c) Al_2O_3 exfoliated from the Al matrix (white arrow).
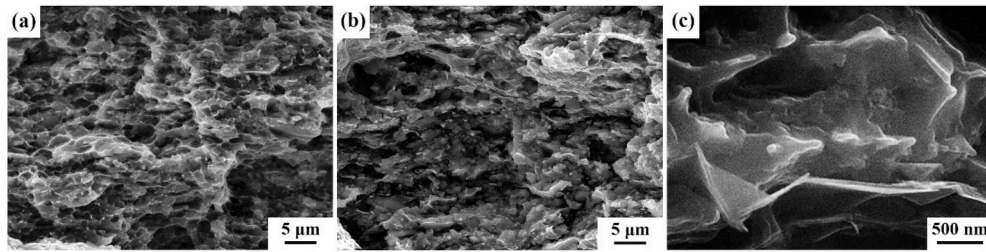
Fig. 11. SEM fractographs of (a) F8 and (b) F16 at 375 °C; (c) high-magnification image showing Al_2O_3 located at grain boundaries in forged samples.
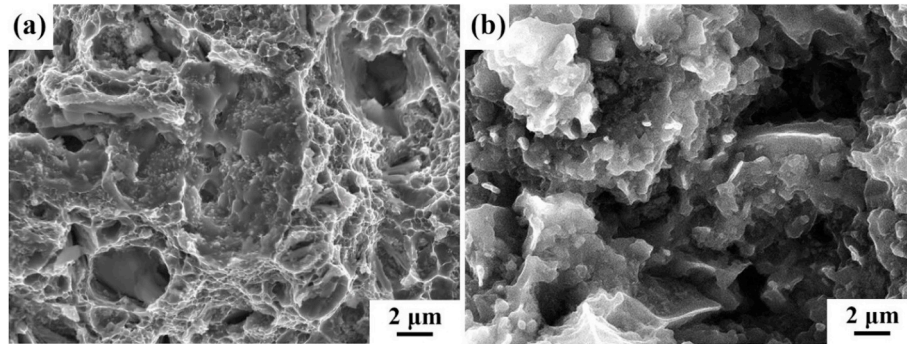

Fig. 12. SEM images showing fracture surfaces (a) at RT and (b) at 375 °C for sample E16.

the fracture surface. It could be speculated that the fracture process initiated at the grain boundaries because of the insufficient high-temperature strength.

4. Discussion

4.1. Strengthening mechanism at RT

By summarizing strengthening mechanisms in the composites, the yield strength of the composites can be expressed as [20]:

$$\sigma_{yc} = \sigma_{ym} + \Delta\sigma_{Al_2O_3} + \Delta\sigma_{B_4C}, \tag{1}$$

where σ_{yc} is the yield strength of the composite, σ_{ym} is the yield strength of Al matrix, $\Delta\sigma_{Al_2O_3}$ is the strength increase coming from Al_2O_3, and $\Delta\sigma_{B_4C}$ is the strength increase coming from B_4C.

The yield strength of Al matrix could be estimated by:

$$\sigma_{ym} = \sigma_o + \frac{K_{HP}}{\sqrt{D}}, \tag{2}$$

where σ_o refers to the friction stress (20 MPa), D is the average grain size, and K_{HP} is the Hall–Petch slope (40 MPa $\sqrt{\mu m}$) [34]. The calculation results of σ_{ym} as well as other values in the following are listed in Table 5.

The strengthening effect of Al_2O_3 comes from two parts: i) direct strengthening by load-transfer ($\Delta\sigma_{L-T}$) and ii) secondary strengthening by dislocation accumulation, including Orowan strengthening ($\Delta\sigma_{Oro}$) and geometrically necessary dislocation (GND) strengthening ($\Delta\sigma_{GND}$)

caused by mismatch in elastic modulus and mismatch in coefficient of thermal expansion [21]. The annealing process before tensile testing makes it reasonable to neglect the strengthening effect of the GNDs caused by mismatch in coefficient of thermal expansion [24,35,36]. So

$$\Delta\sigma_{Al_2O_3} = \Delta\sigma_{Al_2O_3}^{L-T} + \Delta\sigma_{Al_2O_3}^{Oro} + \Delta\sigma_{Al_2O_3}^{GND}. \tag{3}$$

When calculating the $\Delta\sigma_{Al_2O_3}^{L-T}$, the critical length of Al_2O_3 must be taken into consideration. It is considered that Al_2O_3 longer than the critical length can bear its tensile strength during the tensile process, and the critical length of Al_2O_3 (l_c) can be calculated as [37]:

$$l_c = \frac{2t\sigma_R}{\sigma_{ym}}, \tag{4}$$

where t is the thickness of Al_2O_3, σ_R is the strength of Al_2O_3 (3.85 GPa [38]) and σ_{ym} is the yield strength of Al matrix. In this study, the critical length of Al_2O_3 is 856 nm, 706 nm, 494 nm and 733 nm for samples F4, F8, F16 and E16, respectively. Therefore, compared to the Al_2O_3 length as listed in Table 3, for all samples, the critical lengths were longer. According to Ref. [24], $\Delta\sigma_{Al_2O_3}^{L-T}$ can be calculated as:

$$\Delta\sigma_{Al_2O_3}^{L-T} = \frac{L\sigma_{ym}}{4t}V_P, \tag{5}$$

where L is the length of Al_2O_3 and V_p is the volume fraction of Al_2O_3.

For the forged samples, because Al_2O_3 was mainly distributed at the grain boundaries, they cannot effectively increase the strength by means of Orowan mechanism (Fig. 7). For sample E16, as shown in Fig. 8, Al_2O_3 showed Orowan strengthening by pinning dislocations. According to the

Table 5
Prediction of yield strength of $(B_4C + Al_2O_3)$/Al composites at RT.

Sample	σ_{ym}	Al_2O_3			B_4C		Combined prediction	Deviation
		$\Delta\sigma_{L-T}$	$\Delta\sigma_{Oro}$	$\Delta\sigma_{GND}$	$\Delta\sigma_{L-T}$	$\Delta\sigma_{GND}$		
F4	90	49	–	28	5	9	181	77
F8	109	50	–	30	6	9	204	68
F16	156	69	–	31	9	9	274	57
E16	105	15	64	55	6	9	254	8

model proposed by Nie [39], the Orowan strengthening of flaky reinforcement, $\Delta\sigma_{Orowan}$ can be expressed as:

$$\Delta\sigma_{Orowan} = \frac{Gb}{2\pi\sqrt{1-v}}\left(\frac{1}{1.145\sqrt{0.306\pi dt/f} - \pi d\left/8 - 1.061t\right.}\right)ln\frac{0.981\sqrt{dt}}{b},$$

(6)

where G is the shear modulus of aluminium (26.4 GPa), b is the Burgers vector (0.286 nm), v is the Poisson's ratio of Al (0.33), and d, t and f are the average diameter, thickness and volume fraction of reinforcements, respectively.

The yield strength increase caused by GND strengthening ($\Delta\sigma_{GND}$) can be calculated by Ref. [40]:

$$\Delta\sigma_{GND} = \alpha Gb\sqrt{\frac{8V_P\varepsilon_y}{bB}},$$

(7)

where α is the constant that is equal to 1.25, B is the diameter of the prismatic dislocation loop around the particles (approximate to average diameter of reinforcement particles), and ε_y is the yielding strain (0.2%).

For B_4C particles, the Orowan strengthening can be neglected because of their large size, so strengthening effects of B_4C include load-transfer strengthening and GND strengthening. $\Delta\sigma_{B_4C}^{L-T}$ can be calculated as [41]:

$$\Delta\sigma_{B_4C}^{L-T} = 0.5V_P\sigma_{ym}.$$

(8)

The yield strength increase caused by GND strengthening of B_4C can be calculated using Eq. (7). The calculated results and deviations are summarized in Table 5. It can be seen that the prediction of yield strength of sample E16 was relatively accurate with a small deviation of only 8 MPa. However, the deviation in strength prediction of the forged samples was as high as 50–80 MPa. This indicates that the present prediction of strengthening effect of Al_2O_3 in the forged samples remarkably underestimated the experimental values. Therefore, calculations based on the combined effect of load-transfer and dislocation strengthening cannot accurately describe the strengthening effect of the present composites with a lamellar structure. So there should be other strengthening mechanism contributing to the strength enhancement of this lamellar-structured composite.

Considering the different Al_2O_3 distributions in these samples, it is proposed that the extra strengthening in the forged samples originated from Al_2O_3 at the grain boundaries. In general, the grain boundaries act as obstacles for dislocation slip, resulting in the dislocation pile-ups. The plastic yielding occurs once the concentrated stress overcomes the critical value required for activating the slip system in the neighbouring grains [42,43]. The presence of Al_2O_3 at the grain boundaries can largely enhance this critical value. The magnitude of hardening provided by above mechanism can be estimated by Ref. [38]:

$$\Delta\sigma_B = \sqrt{\frac{Gbcos\theta\Delta\sigma_{Al_2O_3}}{\pi(1-\nu)D}},$$

(9)

where $\Delta\sigma_{Al_2O_3}$ is the additional stress that Al_2O_3 can sustain during strain hardening, which was described in Ref. [38], and θ is the angle between the slip plane and the loading axis. By taking θ as 45°, D as lamellae thickness of Al grains, and neglecting the effect of image force, the magnitude of $\Delta\sigma_B$ is obtained as ~80 MPa for sample F4, which can well explain the experimental results. Therefore, it is proven that Al_2O_3 at the grain boundaries in the lamellar structure can enhance the strength by strengthening the grain boundaries.

4.2. Strengthening mechanism at 375 °C

To understand high-temperature deformation behaviour of different samples, the following three factors must be taken into account: i) grain boundary strengthening by pinning effect of Al_2O_3 at the grain

boundaries; ii) dislocation strengthening by climbing mechanism rather than Orowan mechanism at such a high temperature; and iii) L-T strengthening mechanism. These factors will be discussed as follows respectively.

4.2.1. Grain boundary strengthening

It is well known that under high temperature, the grain boundaries would soften and glide easily. Dislocations would annihilate at the grain boundaries by recovery [22]. So the grain boundaries cannot provide strengthening effect any longer as they do at RT.

TEM observation (Fig. 13a) of fractured tensile specimens of sample E16 after tension at 375 °C revealed coarsened grains and obviously decreased dislocation density compared to the as-extruded sample. Dislocations could easily annihilate in the tensile process at the grain boundaries without Al_2O_3 by dynamic recovery. On the contrary, microstructure of sample F8 was quite stable during the high-temperature tensile process with the lamellar structure being preserved (Fig. 13b). In addition, the dark contrast in Fig. 13b indicated the dislocation accumulation in sample F8. This confirmed that the lamellar structure with Al_2O_3 being located at the Al grain boundaries could improve the stability of the grain boundaries and strongly hindered dislocation annihilation, resulting in higher high-temperature strength.

In sample E16, intragranular Al_2O_3 could only hinder a few dislocations which did not climb away from the intersectant glide plane. It was shown that dislocations could not form pile-ups (Fig. 13a and c) and most of them annihilated at the grain boundaries. On the contrary, intergranular Al_2O_3 in the forged samples was exactly located at the grain boundaries. Therefore, dislocations moving to the grain boundaries pinned by Al_2O_3 were stopped and obvious dislocation pile-ups were formed (Fig. 13d). So the dislocation density and grain boundary stability can be enhanced, resulting in higher high-temperature strength.

4.2.2. Dislocation climbing

It was reported that the creep mechanisms became effective above the temperature of 100 °C [22]. At the high temperature of 375 °C (>0.5T_m, where T_m is the absolute melting temperature), dislocations tended to surmount the particles by climbing rather than bypassing [7,23,44].

For composites reinforced by incoherent particles with a low volume fracture, the maximum stress resisting dislocation climb occurs either on the arrival side or at the departure side, resulting in a barrier for dislocation climbing, or a detachment barrier, respectively [45]. And the larger one between these two stresses decides the threshold stress for the whole climb process. The primary cause for this phenomenon is that the line energy of dislocations can be relaxed at the interface between matrix and reinforcements by a factor k (a value between 0 and 1). When k is lower than a critical value, the governing factor in a climb process is the detachment of dislocations, and an attractive interaction can be observed by TEM [46,47].

However, by observing numerous TEM images, such attractive interaction was not found in this study. As shown representatively in Fig. 13c, for intragranular Al_2O_3 in sample E16, dislocations were simply hindered by Al_2O_3. This could be explained by the morphology of Al_2O_3. Compared to particles discussed in Ref. [46], which has more regular and flatter surfaces, the flaky Al_2O_3 is usually curly, so more energy is needed for dislocations to accommodate. So the value of k could be higher. In addition, compared to model analyses of spherical shaped particles in Ref. [45] or cube shaped particles in Ref. [48], the dislocations may need sharper curvatures at the contact point with flaky Al_2O_3, resulting in higher back stress for local climb to initiate [48]. Therefore, the governing factor could be the initiation of climbing. Furthermore, once the dislocations climb to the top of Al_2O_3, unlike the spherical situation, dislocations would not climb back to the original glide plane but begin to detach Al_2O_3. As a result, the attractive interaction was hard to capture.

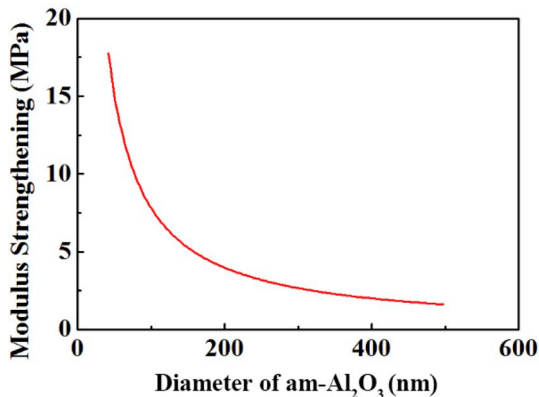The mismatch (modulus mismatch and lattice mismatch) caused by
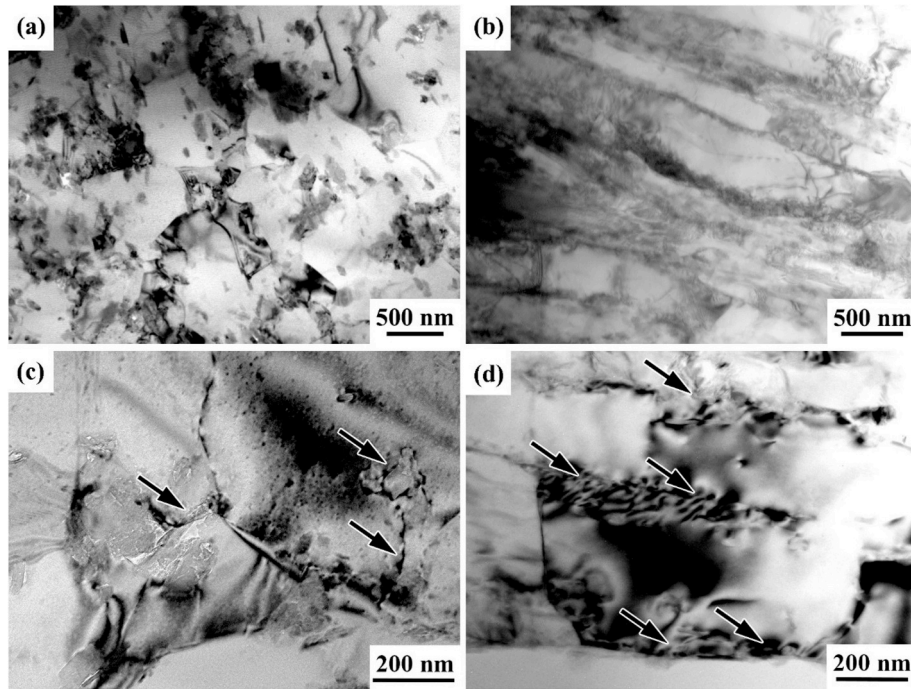
Fig. 13. (a) TEM images showing grain microstructure in samples (a) E16 and (b) F8, and interactions between Al_2O_3 and dislocations in samples (c) E16 and (d) F8 after tensile testing at 375 °C.

reinforcements could lead to higher strain energy and made it harder for dislocations to climb over [7,49,50]. So the strength increment coming from dislocation climbing, $\Delta\sigma_{climbing}$, could be obtained by summing up $\Delta\sigma_{MMC}$ (strength increased by modulus mismatch) and $\Delta\sigma_{LMC}$ (strength increased by lattice mismatch).

$\Delta\sigma_{MMC}$ could be calculated by derivation of the interaction energy for a unit length of an edge dislocation with the reinforcements. According to the equation given in Refs. [7,49], the $\Delta\sigma_{MMC}$-diameter curve is given in Fig. 14 (taking shear modulus of Al at 375 °C as 21 GPa [7], shear modulus of Al_2O_3 as 141 GPa [51], Poisson's ratio of Al as 0.33 [7], Poisson's ratio of Al_2O_3 as 0.2 [51]). Although some error might exist because of the complexity of strength predicting at high temperature, it is clear that the tendency is totally unconformable to the experimental results, because shorter Al_2O_3 would lead to higher $\Delta\sigma_{MMC}$ by calculation. So $\Delta\sigma_{MMC}$ was not responsible for the higher strength of the forged samples.

As for $\Delta\sigma_{LMC}$, it can be expressed as [7]:

$$\Delta\sigma_{LMC} = M\chi(\varepsilon G)^{3/2}(rV_P b/\Gamma)^{1/2}, \tag{10}$$

Fig. 14. Curve showing strength increased by modulus mismatch (Modulus strengthening) vs. diameter of am-Al_2O_3.

where χ is a constant, ε is a parameter proportional to lattice parameter mismatch, G is the shear modulus of Al, and Γ can be expressed as:

$$\Gamma = 2Gb\varepsilon r \tag{11}$$

It can be seen that $\Delta\sigma_{LMC}$ is mainly related to the lattice parameter mismatch. However, Al_2O_3 in these samples was mainly amorphous according to the TEM images (Fig. 4c). So the difference in $\Delta\sigma_{LMC}$ can be neglected in this study.

4.2.3. Load-transfer strengthening

By Eq. (5), taking σ_{ym} of Al matrix at 375 °C as 18 MPa [7], the $\Delta\sigma_{L-T}$ of samples F8 and E16 are only 8 MPa and 2 MPa. A disparity of only 6 MPa shows that the load-transfer strengthening is not enough to explain the significant distinction of the actual strengths. Furthermore, it was reported that the efficiency of load-transfer strengthening may be decreased at high temperature because of diffusional assisted flow [52].

Based on the results and analysis, a schematic can be summarized to generalize the high-temperature tensile behaviour in the two microstructures, as shown in Fig. 15. At high temperatures, strengthening the grain boundaries to maintain their stability played a vital role for high-temperature strength [22,53]. Al_2O_3 located exactly at the grain boundaries is more effective than intragranular Al_2O_3 in strengthening the Al matrix by strengthening the grain boundaries and preventing dislocations from annihilating, as shown in Fig. 13b, d and 15a. For sample E16 (Fig. 13a, c and 15b), intragranular Al_2O_3 can only pin a few dislocations but cannot strengthen the grain boundaries, so dislocations annihilate easily at the grain boundaries. The grain boundaries would slide and then be broken under the effect of shearing stress [22,28]. Therefore, in the forged samples, the lamellar structure was quite stable; but for the extruded sample, fracture happened at the grain boundaries, so obvious intergranular fracture was found, which was in accordance with the fracture behaviours shown in Figs. 11 and 12. As a result, the forged samples were much stronger than the extruded sample at 375 °C. So making Al_2O_3 distributed at the grain boundaries is an effective way to increase the high-temperature strengthening efficiency of Al_2O_3 in SAPs.

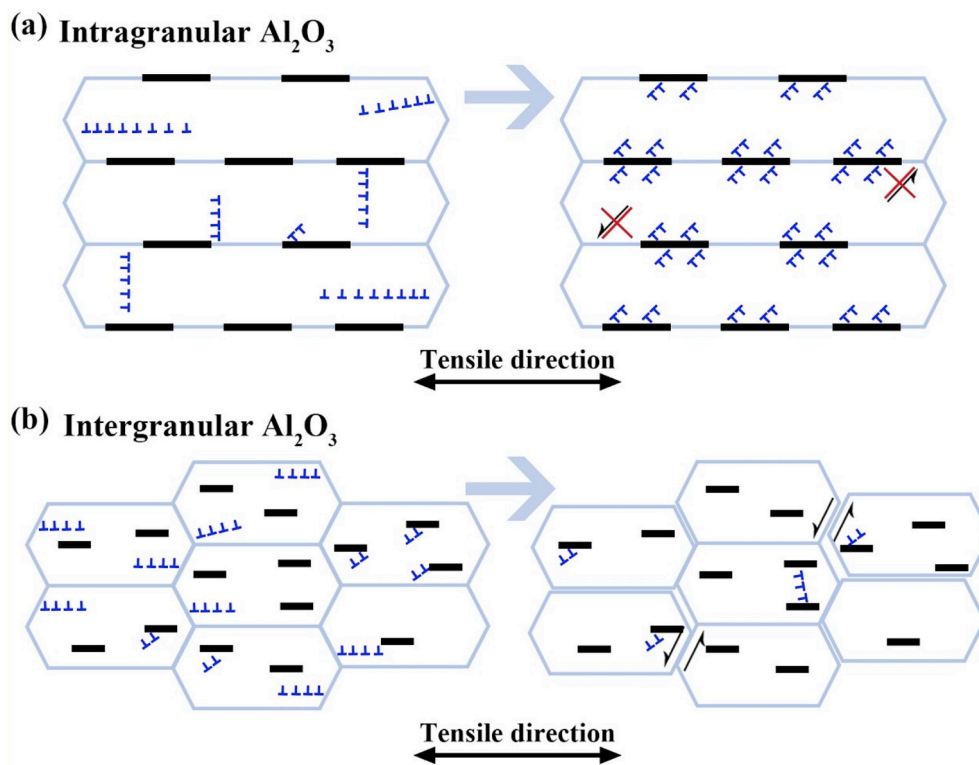SAPs prepared from the ball-milled flaky Al powders were usually

Fig. 15. Schematic drawings of strenghthening of (a) intragranular and (b) intergranular Al_2O_3 in the tensile process.

compacted using extrusion in 1950s, so it could be speculated that these SAPs exhibited the ultrafine-grained microstructure similar to sample E16 in this study. Sample E16 showed a similar strength to S.A.P. 930 (ordinary SAP with 7 wt% Al_2O_3) [19], while sample F8 with the lamellar structure showed a similar strength to S.A.P. 895 (ordinary SAP with 10 wt% Al_2O_3) [19]. Thus, it is proven that by constructing the lamellar structure, the strengthening efficiency of Al_2O_3 was increased and competent high-temperature strength was obtained using a lower content of only 5.8 vol% Al_2O_3 (6.2 wt% Al_2O_3).

5. Conclusions

In this work, $(B_4C + Al_2O_3)/Al$ composites designed for structural neutron absorbing materials were fabricated using powder metallurgy method, followed by forging and extrusion. The strengthening mechanisms of Al_2O_3 at room temperature (RT) and 375 °C were studied with both direct strengthening and secondary strengthening being taken into consideration. The following conclusions are made:

(1) The difference in the plastic working modes resulted in significant variations in the microstructures of the composites. The forged samples exhibited a lamellar structure with Al_2O_3 300–400 nm in the average length being located at the lamella boundaries, while the extruded sample exhibited an ultrafine-grained structure and intragranular Al_2O_3 with the average length smaller than 100 nm was observed.

(2) Al_2O_3 exhibited obvious strengthening effect at RT and 375 °C. At RT, sample F16 (16:1 forging reduction ratio) exhibited the highest tensile strength (369 MPa), and sample E16 (16:1 extrusion ratio) exhibited similar tensile strength with sample F8 (8:1 forging reduction ratio) (326 MPa and 342 MPa). At 375 °C, sample F8 exhibited the highest tensile strength (96 MPa) but the strength of E16 (58 MPa) was far lower than that of the forged samples.

(3) At RT, the strength could be increased by both forging and extrusion. The strengthening mechanisms of Al_2O_3 included load-transfer strengthening and dislocation strengthening. For the forged samples, extra strengthening effect of intergranular Al_2O_3 in the lamellar structure was confirmed and interpreted as enhancing the inhibition effect of grain boundaries on dislocation slip.

(4) At 375 °C, Al_2O_3 in the lamellar structure could improve the stability of the grain boundaries and strongly hindered dislocation annihilation, resulting in that the forged samples exhibited a higher strength than the extruded sample. It was proven that constructing the lamellar structure with intergranular Al_2O_3 was an effective approach for enhancing the high-temperature strength.

Data availability

The raw/processed data will be made available on request.

Declaration of competing interest

The authors declare that they have no known competing financial interests or personal relationships that could have appeared to influence the work reported in this paper.

CRediT authorship contribution statement

Acknowledgments

Appendix A. Supplementary data

Supplementary data to this article can be found online at https://doi.org/10.1016/j.compositesb.2019.107674.

References

[1] Xu ZG, Jiang LT, Zhang Q, Qiao J, Gong D, Wu GH. The design of a novel neutron shielding B_4C/Al composite containing Gd. Mater Des 2016;111:375–81.

[2] Zhou Y, Zan Y, Zheng S, Shao X, Jin Q, Zhang B, et al. Thermally stable microstructures and mechanical properties of B_4C-Al composite with in-situ formed $Mg(Al)B_2$. J Mater Sci Technol 2019;35(9):1825–30.

[3] Jiang LT, Xu ZG, Fei YK, Zhang Q, Qiao J, Wu GH. The design of novel neutron shielding $(Gd+B_4C)/6061Al$ composites and its properties after hot rolling. Composites Part B 2019;168:183–94.

[4] Chao ZL, Jiang LT, Chen GQ, Qiao J, Z Q, Yu ZH, et al. The microstructure and ballistic performance of $B_4C/AA2024$ functionally graded composites with wide range B_4C volume fraction. Composites Part B 2019;161:627–38.

[5] Ş Karabulut, Karakoç H, Çıtak R. Influence of B_4C particle reinforcement on mechanical and machining properties of Al6061/B_4C composites. Composites Part B 2016;101:87–98.

[6] Zan YN, Zhang Q, Zhou YT, Wang QZ, Xiao BL, Ma ZY. Enhancing high-temperature strength of B_4C–6061Al neutron absorber material by in-situ $Mg(Al)$ B_2. J Nucl Mater 2019;526:151788.

[7] Qin J, Zhang Z, Chen XG. Mechanical properties and strengthening mechanisms of Al-15 Pct B_4C composites with Sc and Zr at elevated temperatures. Metall Mater Trans A 2016;47(9):4694–708.

[8] Chen XG, St-Georges L, Roux M. Mechanical behavior of high boron content Al-B_4C metal matrix composites at elevated temperatures. Thermec 2011;706–709:631–7. Pts 1-4 2012.

[9] Junaedi H, Ibrahim MF, Ammar HR, Samuel AM, Soliman MS, Almajid AA, et al. Effect of testing temperature on the strength and fracture behavior of Al-B_4C composites. J Compos Mater 2016;50(20):2871–80.

[10] Feng J, Ye B, Zuo LJ, Qi RJ, Wang QD, Jiang HY, et al. Effects of Ni content on low cycle fatigue and mechanical properties of Al-12Si-0.9Cu-0.8Mg-xNi. at 350 °C. Mater Sci Eng A 2017;706:27–37.

[11] Li GJ, Liao HC, Suo XJ, Tang YY, Dixit US, Petrov P. Cr-induced morphology change of primary Mn-rich phase in Al-Si-Cu-Mn heat resistant aluminum alloys and its contribution to high temperature strength. Mater Sci Eng A 2018;709:90–6.

[12] Hu K, Xu Q, Ma X, Sun Q, Gao T, Liu X. A novel heat-resistant Al–Si–Cu–Ni–Mg base material synergistically strengthened by Ni-rich intermetallics and nano-AlN_p microskeletons. J Mater Sci Technol 2019;35(3):306–12.

[13] Suo XJ, Liao HC, Hu YY, Dixit US, Petrov P. Formation of $Al_{15}Mn_3Si_2$ phase during solidification of a novel Al-12%Si-4%Cu-1.2%Mn heat-resistant alloy and its thermal stability. J Mater Eng Perform 2018;27(6):2910–21.

[14] Morri A, Ceschini L, Messieri S, Cerri E, Toschi S. Mo addition to the A354 (Al-Si-Cu-Mg) casting alloy: effects on microstructure and mechanical properties at room and high temperature. Metals 2018;8(6):18.

[15] Ceschini L, Morri A, Toschi S, Seifeddine S. Room and high temperature fatigue behaviour of the A354 and C355 (Al-Si-Cu-Mg) alloys: role of microstructure and heat treatment. Mater Sci Eng A 2016;653:129–38.

[16] Wang P, Gammer C, Brenne F, Niendorf T, Eckert J, Scudino S. A heat treatable TiB_2/Al-3.5Cu-1.5Mg-1Si composite fabricated by selective laser melting: microstructure, heat treatment and mechanical properties. Composites Part B 2018;147:162–8.

[17] Machiels A, Lanmbert R. Handbook of neutron absorber materials for spent nuclear fuel transportation and storage applications. California: Electric Powder Research Institute; 2009.

[18] Meyersa CL, Stulpe K. Metallographic evidence of the existence of a continuous-oxide phase in SAP-865. Metallography 1969;2(1):41–56.

[19] Bloch EA. Dispersion-strengthened aluminium alloys. Metall Rev 1961;6(1):193–240.

[20] Kai XZ, Li ZQ, Fan GL, Guo Q, Xiong DB, Zhang WL, et al. Enhanced strength and ductility in particulate-reinforced aluminum matrix composites fabricated by flake powder metallurgy. Mater Sci Eng A 2013;587:46–53.

[21] Chawla N, Shen YL. Mechanical behavior of particle reinforced metal matrix composites. Adv Eng Mater 2001;3(6):357–70.

[22] Poletti C, Balog M, Simancik F, Degischer HP. High-temperature strength of compacted sub-micrometer aluminium powder. Acta Mater 2010;58(10):3781–9.

[23] Zhu SM, Tjong SC, Lai JKL. Creep behavior of a β'(NiAl) precipitation strengthened ferritic Fe–Cr–Ni–Al alloy. Acta Mater 1998;46(9):2969–76.

[24] Nardone VC, Prewo KM. On the strength of discontinuous silicon carbide reinforced aluminum composites. Scr Metall 1986;20(1):43–8.

[25] Campbell T, Kalia RK, Nakano A, Vashishta P, Ogata S, Rodgers S. Dynamics of oxidation of aluminum nanoclusters using variable charge molecular-dynamics simulations on parallel computers. Phys Rev Lett 1999;82(24):4866–9.

[26] Zan YN, Zhou YT, Liu ZY, Ma GN, Wang D, Wang QZ, et al. Enhancing strength and ductility synergy through heterogeneous structure design in nanoscale Al_2O_3 particulate reinforced Al composites. Mater Des 2019;166:107629.

[27] Trinh PV, Luan NV, Phuong DD, Minh PN, Weibel A, Mesguich D, et al. Microstructure, microhardness and thermal expansion of CNT/Al composites prepared by flake powder metallurgy. Compos Appl Sci Manuf 2018;105:126–37.

[28] Balog M, Hu T, Krizik P, Castro Riglos MV, Saller BD, Yang H, et al. On the thermal stability of ultrafine-grained Al stabilized by in-situ amorphous Al_2O_3 network. Mater Sci Eng A 2015;648:61–71.

[29] Balog M, Poletti C, Simancik F, Walcher M, Rajner W. The effect of native Al_2O_3 skin disruption on properties of fine Al powder compacts. J Alloy Comp 2011;509: S235–8.

[30] Jeurgens LPH, Sloof WG, Tichelaar FD, Mittemeijer EJ. Thermodynamic stability of amorphous oxide films on metals: application to aluminum oxide films on aluminum substrates. Phys Rev B 2000;62(7):4707–19.

[31] Zhou YT, Zan YN, Zheng SJ, Wang QZ, Xiao BL, Ma XL, et al. Distribution of the microalloying element Cu in B_4C-reinforced 6061Al composites. J Alloy Comp 2017;728(Supplement C):112–7.

[32] Yu CY, Kao PW, Chang CP. Transition of tensile deformation behaviors in ultrafine-grained aluminum. Acta Mater 2005;53(15):4019–28.

[33] Chen HS, Wang WX, Li YL, Zhou J, Nie HH, Wu QC. The design, microstructure and mechanical properties of B_4C/6061Al neutron absorber composites fabricated by SPS. Mater Des 2016;94:360–7.

[34] Alizadeh M, beni HA. Strength prediction of the ARBed Al/Al_2O_3/B_4C nano-composites using Orowan model. Mater Res Bull 2014;59:290–4.

[35] Arsenault RJ, Fisher RM. Microstructure of fiber and particulate SiC in 6061 Al composites. Scr Metall 1983;17(1):67–71.

[36] Cho H-H, Hong S-T, Roh J-H, Choi H-S, Kang SH, Steel RJ, et al. Three-dimensional numerical and experimental investigation on friction stir welding processes of ferritic stainless steel. Acta Mater 2013;61(7):2649–61.

[37] Zhang ZW, Liu ZY, Xiao BL, Ni DR, Ma ZY. High efficiency dispersal and strengthening of graphene reinforced aluminum alloy composites fabricated by powder metallurgy combined with friction stir processing. Carbon 2018;135: 215–23.

[38] Li S-H, Han W-Z, Li J, Ma E, Shan Z-W. Small-volume aluminum alloys with native oxide shell deliver unprecedented strength and toughness. Acta Mater 2017;126: 202–9.

[39] Nie JF, Muddle BC. Strengthening of an Al–Cu–Sn alloy by deformation-resistant precipitate plates. Acta Mater 2008;56(14):3490–501.

[40] Tang F, Anderson IE, Gnaupel-Herold T, Prask H. Pure Al matrix composites produced by vacuum hot pressing: tensile properties and strengthening mechanisms. Mater Sci Eng A 2004;383(2):362–73.

[41] Zhang Z, Chen DL. Consideration of Orowan strengthening effect in particulate-reinforced metal matrix nanocomposites: a model for predicting their yield strength. Scr Mater 2006;54(7):1321–6.

[42] Maung K, Earthman JC, Mohamed FA. Inverse Hall–Petch behavior in diamantane stabilized bulk nanocrystalline aluminum. Acta Mater 2012;60(16):5850–7.

[43] Hall EO. The deformation and ageing of mild steel: III discussion of results. Proc Phys Soc Sect B 1951;64(9):747–53.

[44] Tian WS, Zhao QL, Zhang QQ, Jiang QC. Simultaneously increasing the high-temperature tensile strength and ductility of nano-sized TiC_p reinforced Al-Cu matrix composites. Mater Sci Eng A 2018;717:105–12.

[45] Arzt E, Wilkinson DS. Threshold stresses for dislocation climb over hard particles - the effect of an attractive interaction. Acta Metall 1986;34(10):1893–8.

[46] Behr R, Mayer J, Arzt E. TEM investigations of the superdislocations and their interaction with particles in dispersion strengthened intermetallics. Intermetallics 1999;7(3–4):423–36.

[47] Schröder JH, Arzt E. Weak beam studies of dislocation/dispersoid interaction in an ods superalloy. Scr Metall 1985;19(9):1129–34.

[48] Lagneborg R. Bypassing of dislocations past particles by a climb mechanism. Scr Metall 1973;7(6):605–13.

[49] Marquis EA, Dunand DC. Model for creep threshold stress in precipitation-strengthened alloys with coherent particles. Scr Mater 2002;47(8):503–8.

[50] Ardell AJ. Precipitation hardening. Metall Trans A 1985;16(12):2131–65.

[51] Davis S, Gutierrez G. Structural, elastic, vibrational and electronic properties of amorphous Al_2O_3 from ab initio calculations. J Phys Condens Matter 2011;23(49): 495401.

[52] Wang SH, Kao PW. The strengthening effect of Al_3Ti in high temperature deformation of Al-Al3Ti composites. Acta Mater 1998;46(8):2675–82.

[53] Balog M, Simancik F, Walcher M, Rajner W, Poletti C. Extruded Al-Al_2O_3 composites formed in situ during consolidation of ultrafine Al powders: effect of the powder surface area. Mater Sci Eng A 2011;529:131–7.